An Investigation into Non-Linear Growth Rate of 2D and 3D Single-Mode Richtmyer–Meshkov Instability

Mike Probyn
Centre for Fluid Mechanics
and Scientific Computing
School of Engineering
Cranfield University
MK43 0AL, United Kingdom
Email: m.g.probyn@cranfield.ac.uk

Ben Thornber
School of Aerospace, Mechanical
and Mechatronic Engineering
Faculty of Engineering and Information Technologies
University of Sydney
NSW, Australia
Email: ben.thornber@sydney.edu.au

Dimitris Drikakis
Centre for Fluid Mechanics
and Scientific Computing
School of Engineering
Cranfield University
MK43 0AL, United Kingdom
Email: d.drikakis@cranfield.ac.uk

David Youngs
AWE, Aldermaston
Reading
RG7 4PR, United Kingdom
Email: david.youngs@awe.co.uk

Robin Williams
AWE, Aldermaston
Reading
RG7 4PR, United Kingdom
Email: robin.williams@awe.co.uk

This paper presents an investigation into the use of a moving mesh algorithm for solving unsteady turbulent mixing problems. The growth of a shock induced mixing zone following reshock, using an initial setup comparable to that of existing experimental work, is used to evaluate the behaviour of the numerical scheme for single-mode Richtmyer–Meshkov instability.

Subsequently the code is used to evaluate the growth rate for a range of different initial conditions. The initial growth rate for 3D single-mode Richtmyer–Meshkov is also presented for a number of different initial conditions. This numerical study details the development of the mixing layer width both prior to and after reshock.

The numerical scheme used includes an arbitrary Lagrangian-Eulerian grid motion which is successfully used to reduce the mesh size and computational time whilst retaining the accuracy of the simulation results. Varying initial conditions shows that the growth rate after reshock is indepedent of the initial conditions for a single-mode providing that the initial growth remains in the linear regime.

1 Introduction

Richtmyer–Meshkov instability (RMI) occurs when a shock passes through a perturbed interface between two fluids [1, 2]. The misalignment of pressure and density gradient causes the deposition of vorticity, which promotes turbulent mixing. RMI is observed in a variety of phenomena ranging from supernovae to inertial confinement fusion (ICF) [3, 4].

In the case of convergent geometries, such as inertial confinement fusion, the shock wave will be reflected from

the central focal point. This reflected wave may interact with the mixing layer causing deposition of yet more vorticity. A number of models of reshock have been proposed and work by Latini *et al.* [5] compares numerical results to the experimental work by Collins and Jacobs [6].

This paper investigates Richtmyer–Meshkov instability in shock-tubes using a novel algorithm. This is done to validate the algorithm used and to test a moving mesh technique which has been implemented into the existing Cranfield in-house code, CHOC (see Section 2 for full details). The moving mesh technique is useful for reshock and convergent geometries whereby the region of interest moves considerably. Using this method cells can be clustered around regions of interest and track the interfaces without the computational penalty of using a highly refined grid throughout the domain. Here the algorithm is validated for a number of cases including the Sod-shock [7] tube case and the single-mode Richtmyer–Meshkov instability (SM-RMI) case compared with the results of Collins and Jacobs [6].

2 Numerical Methods

The Cranfield in-house code CHOC (Compressible High Order Code) used in this study is an implicit large-eddy simulation (ILES) code [8]. The code can be used to solve the viscous equations, however, for the purpose of this work an inviscid solver is used based on the Euler equations

$$\frac{\partial \mathbf{U}}{\partial t}+\frac{\partial \mathbf{E}}{\partial x}+\frac{\partial \mathbf{F}}{\partial y}+\frac{\partial \mathbf{G}}{\partial z}=0\,, \tag{1}$$

with the corresponding components defined as

$$\mathbf{U}=(\rho,\rho u,\rho v,\rho w,E)^T\,, \tag{2a}$$
$$\mathbf{E}=(\rho u,p+\rho u^2,\rho uv,\rho uw,u(E+p))^T\,, \tag{2b}$$
$$\mathbf{F}=(\rho v,\rho uv,p+\rho v^2,\rho vw,v(E+p))^T\,, \tag{2c}$$
$$\mathbf{G}=(\rho w,\rho uw,\rho vw,p+\rho w^2,w(E+p))^T\,, \tag{2d}$$

where the usual definitions are used, i.e. ρ is the density, u,v and w represent the velocities in x,y and z, respectively, p and E are the pressure and total energy. Cartesian co-ordinates x,y,z are used with corresponding computational indices i,j and k. The direction of shock propagation in time (t) is x in the following simulations.

The total energy is the sum of the internal energy and kinetic energy written as

$$E=\rho\left(\frac{1}{2}(u^2+v^2+w^2)+e\right)\,, \tag{3}$$

and internal energy (e) is given by the perfect gas equation of state

$$e=\frac{p}{\rho(\gamma-1)}\,, \tag{4}$$

where γ is the ratio of the specific heats.

The equations are modified for multispecies flow using the volume fraction method of Allaire [9]. This method replaces the continuity equation with two equations for the volume fraction (α) and density of each species, and adds an additional (non-conservative) equation for the advection of volume fraction. These additional equations are

$$\frac{\partial \rho_1\alpha_1}{\partial t}+\frac{\partial \rho_1\alpha_1 u}{\partial x}+\frac{\partial \rho_1\alpha_1 v}{\partial y}+\frac{\partial \rho_1\alpha_1 w}{\partial z}=0\,, \tag{5a}$$
$$\frac{\partial \rho_2\alpha_2}{\partial t}+\frac{\partial \rho_2\alpha_2 u}{\partial x}+\frac{\partial \rho_2\alpha_2 v}{\partial y}+\frac{\partial \rho_2\alpha_2 w}{\partial z}=0\,, \tag{5b}$$
$$\frac{\partial \alpha_1}{\partial t}+u\frac{\partial \alpha_1}{\partial x}+v\frac{\partial \alpha_1}{\partial y}+w\frac{\partial \alpha_1}{\partial z}=0\,. \tag{5c}$$

The governing equations, Eq. (1), are converted into a computational coordinate domain (ξ,η,ζ and time τ) and a moving mesh velocity in the ξ direction (μ) is incorporated. The Jacobian (J) is used to transform between co-ordinate systems. Since the mesh moves the Jacobian differs between time-steps (n). The resulting equation (shown in 1D for simplicity) yields

$$\frac{\partial J\mathbf{U}}{\partial \tau}+\frac{\partial J\frac{\partial \xi}{\partial x}(\mathbf{E}-\mu\mathbf{U})}{\partial \xi}=0\,. \tag{6}$$

It can be seen that the Jacobian is included is the time derivative. This equation is subsequently discretized (in the example here Euler time-stepping is used) to yield

$$\mathbf{U}^{n+1}=\frac{J^n}{J^{n+1}}\mathbf{U}^n+\frac{\Delta t}{J^{n+1}}\mathbf{F}(\hat{\mathbf{U}}^n)\,, \tag{7}$$

where $\hat{\mathbf{U}}=\frac{\partial \xi}{\partial x}(\mathbf{E}-\mu\mathbf{U})$, i.e. the fluxes are modified by the moving grid velocity and the conversion to computational coordinates. As a consequence of this the first term of the right-hand side of Eq. (7) contains a factor of J^n/J^{n+1}, this arises from the Jacobian existing in the time derivative and does not occur in a standard stationary mesh algorithm.

The main novelty of the present work is in the discretization of the volume fraction equation (Eq. (5c)) for a moving mesh. Since this equation is non-conservative in nature the result when converted from cartesian to computational coordinates is not the same as Eq. (6). Instead the result is

$$\frac{\partial (J\alpha_1)}{\partial \tau}-\alpha_1\frac{\partial J}{\partial \tau}+(\mu+u)\frac{\partial (J\frac{\partial \xi}{\partial x}\alpha_1)}{\partial \xi}=0\,. \tag{8}$$

In this equation there are two terms relating the Jacobian to the time derivative, discretization using the Euler time-stepping yields

$$\alpha_1^{n+1} = \alpha_1^n - \frac{\Delta t}{\Delta x}(\mu + u)\frac{(J\frac{\partial \xi}{\partial x}\alpha_1)_{i+1/2} - (J\frac{\partial \xi}{\partial x}\alpha_1)_{i-1/2}}{J^{n+1}} . \quad (9)$$

This is comparable to Eq. (7) for a non-conservative formulation. This form also requires some modification based on the moving grid velocity and the transformation to computational coordinates, however there is no multiplication of the first term of the right-hand side by the different Jacobians, hence the non-conservative equations undergo a slightly modified time-stepping procedure.

This completes the description of the moving mesh algorithm. It allows the grid to move with an arbitrary velocity, offering the advantage of being able to cluster cells in the regions of interest and advect the high resolution grid with the flow. Any grid velocity can be prescribed.

In practice, to maintain an orthogonal mesh, all nodes with the same i index are moved at the average velocity at that plane $x = x_i$ (assuming that the shock propagates in the x_i direction). This means that the clustering will always remain around the interface.

The equations are discretized using a 5^{th} order in space MUSCL scheme [10] and a 2^{nd} order accurate in time Runge-Kutta method [11] using a low Mach corrected Godunov method [12, 13]. The HLLC Riemann solver is implemented as shown in Toro [14].

3 Discussion

3.1 Moving Grid Validation

To test the behaviour of the moving mesh code, a simple 1D Sod-shock [7] test case was used. Standard initial conditions are used with density, pressure and velocity given as (1.0,1.0,0.0) and (0.125,0.1,0.0) for the left and right states, respectively. The initial interface is at $x = 0.5$ in a domain $0.0 < x < 1.0$ comprised of 100 cells. Two different fluids are assumed for the left and right states with volume fraction 0.0 and 1.0 applied respectively. A single ratio of specific heats ($\gamma = 1.4$) is used for both gases. The boundary conditions at $x = 0.0$ and $x = 1.0$ are outflows.

Figure 1 shows the development of the density over time comparing the stationary and moving mesh algorithms with the exact solution. In Fig. 1a the initial conditions are shown followed by snapshots at $t = 0.2$s and $t = 0.4$s in Fig. 1b and Fig. 1c, respectively. From these it can be seen that the moving grid behaves well, without generating spurious oscillations and that the contact surface is preserved with a greater accuracy in the moving mesh case. Further improvements in accuracy can be achieved by clustering cells around the interesting areas and this will be investigated in Sec. 3.2.

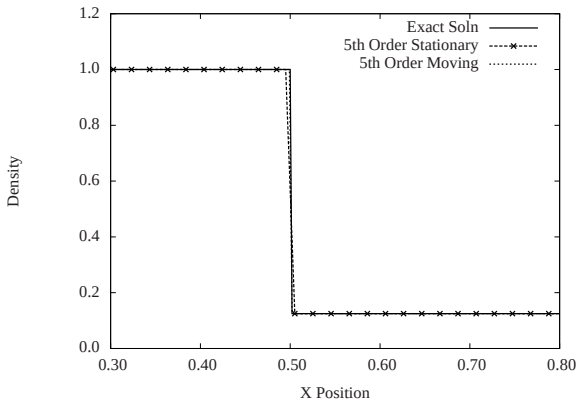

(a) 0.0s

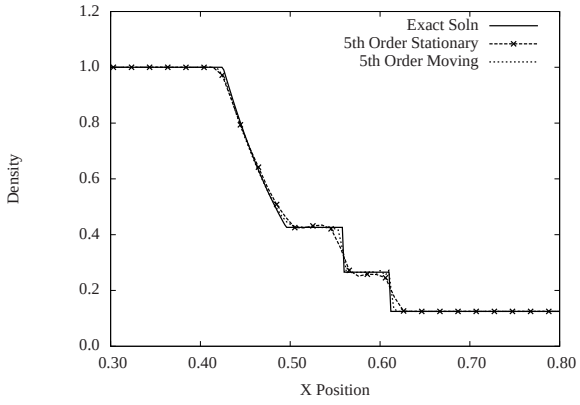

(b) 0.2s

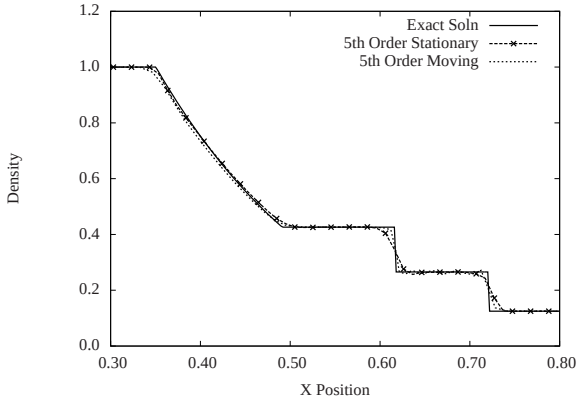

(c) 0.4s

Fig. 1: Development of the density field with time for the Sod-shock tube test case comparing stationary and moving grid algorithms

3.2 2D Grid Study

To evaluate the required resolution to achieve consistent results, a grid study was undertaken. A test case was set up in accordance with the initial conditions of the work of Collins and Jacobs [6]. The experiment consisted of two fluids, air/acetone (75% air and 25% acetone as a tracer) and SF_6 with the interface placed 750mm from the endwall. A

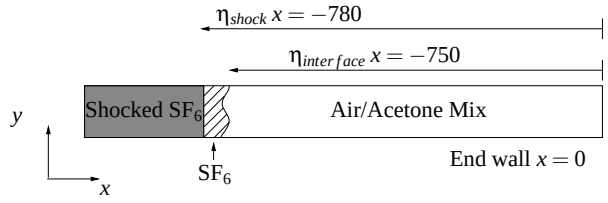

Fig. 2: Schematic of the simulation based on the Collins and Jacobs experiment. The end wall is at $x = 0$ whilst the opposite x boundary is an extended domain to allow outflow without additional pressure waves polluting the solution. The remaining boundary conditions are treated as inviscid (slip) walls. The domains is 89mm in length and the single-mode perturbation has a wavelength of 59mm with an initial amplitude of 2mm

shock of Mach number 1.21 travelled from the heavy gas (SF_6) into the light gas (air). The test chamber had a cross section of 89mm and there is a single-mode (SM) perturbation with a wavelength of 59mm and initial (pre-shock) amplitude of $\sim$ 2mm. The experiment has a diffuse initial interface estimated in [6] to be $\sim$ 5mm.

The simulation uses the same geometry and gas specifiaction and is initialised with a section of the SF_6 having the properties of the shocked fluid at 780mm from the end wall. These properties are calculated from the normal shock relations.

Inviscid (slip) wall boundary conditions are used along the length of the simulated shock tube. The simulation end wall is also an inviscid wall to ensure that a reshock occurs at the appropriate time as in the experiment. The final edge is left as an outflow to prevent pollution of the solution as the flow leaves the domain. The computational set up is shown schematically in Fig. 2 showing the position of the initial shock and interface relative to the end wall.

A stationary grid and a moving grid were both evaluated. The number of cells in the stationary grid was doubled in both the transverse and shock propagation directions. The cases are labelled as S1 (64 x 512 cells), S2 (128 x 1024 cells), S3 (256 x 2048 cells) and S4 (512 x 4096). The results for the width of the mixing layer are plotting against time to a point past reshock. A moving grid test case was also used with the same number of cells in the transverse direction but using a quarter of the corresponding cells in the shock direction, clustered around the regions of interest, these grids are labelled as M1 (64 x 128 cells), M2 (128 x 256 cells) and M3 (256 x 512 cells).

These data are presented to establish the accuracy of the results with two aims, firstly to demonstrate that the mixing layer width becomes independent of the grid resolution and secondly that the use of the moving grid produces similar results to those of the stationary code. The mixing width is used as a measure of the growth of the instability and is defined as $W = \max(x_{\alpha=0.5}) - \min(x_{\alpha=0.5})$.

Figure 3a shows a comparison of the mixing width for stationary algorithm results at different grid resolutions.

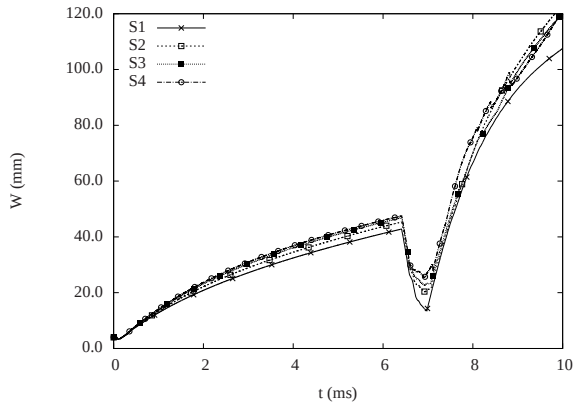

(a) Stationary grid resolution study, resolutions of 64, 128, 256 and 512 cells in the y direction

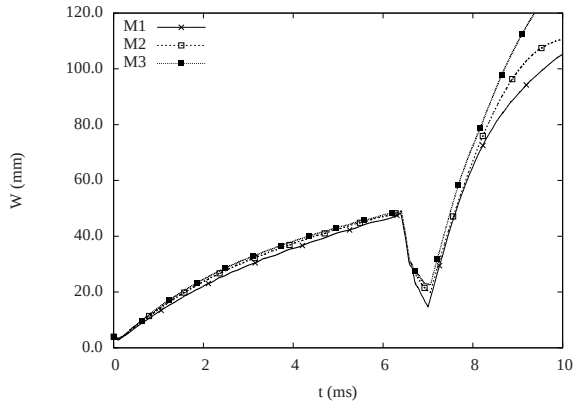

(b) Moving grid resolution study, cases are same resolution in the y direction as the corresponding stationary cases, whereas 1/4 of the cells are used in the x (shock) direction

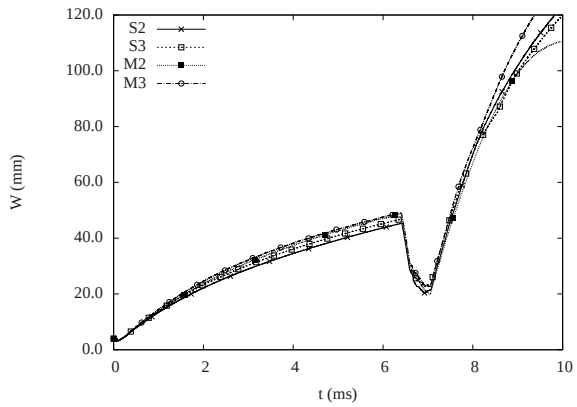

(c) Comparison of stationary and moving grid results

Fig. 3: Results of 2D grid study comparing stationary and moving grid techniques for mixing layer width development as a function of time

Prior to reshock (around 6ms reshock initially compresses the layer as it passes) there is reasonable agreement between all three resolutions, though the lowest resolution is appreciably lower than the other results. Immediately after reshock there is excellent agreement between all three

cases, though at late-time (after 8ms) the lowest resolution tends to fall away. Figure 3a suggests that the solution becomes grid independent at around the S2 resolution. At late time the S4 resolution suffers from high disturbances due to Kelvin–Helmholtz instability (KHI), frequently observed on very fine meshes as shown by Mosedale [15].

It should be noted that it is difficult to replicate late-time results for 2D cases since the flow becomes dominated by large scale vortex motion. The results are then highly sensitive to the structure and position of these vortices, which do not break down into homogeneous decaying turbulence. The difference is shown well in Fig. 4 which compares the S1 and S4 cases showing the large scale vortices in Fig. 4a (the lowest resolution case) and the KHI in Fig. 4b.

Next the different moving mesh resolutions are compared in Fig. 3b. Here again it can be seen that there is excellent agreement prior to reshock and immediately after reshock, however, at late-time the results again vary for the reasons outlined previously.

The most interesting comparison is shown in Fig. 3c where the results of the stationary mesh are compared to the moving mesh case. Note here that the lowest resolution cases (S1 and M1) have been omitted for clarity, because they are not sufficiently high resolution to become grid independent even before $t = 8$ms. This moving mesh algorithm has been validated against a stationary grid case and displays convergence using only 1/4 of the cells in the shock direction compared to the stationary case.

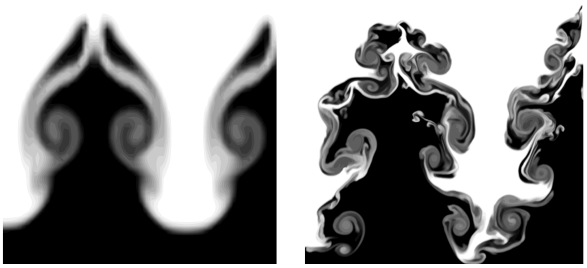

(a) Lowest resolution (S1) (b) Highest resolution (S4)

Fig. 4: Comparison of contour plots of volume fraction for the 2D results for the highest and lowest resolution case at 9ms. The large scale vortical structures can be seen in the lowest resolution case and the additional smaller scale vortices arising from KHI are visible at the higher resolution

3.3 3D Testing

A number of 3D cases were tested, also based on the Collins and Jacobs experiment, using the moving mesh algorithm.

A 3D single-mode case is a 3D simulation with the initial conditions exactly as in 2D but extrapolated in the third dimension. Two perturbed-mode cases were also tested consisting of the dominant single-mode with additional perturbed modes superposed into the initial conditions. The first of these perturbed-mode cases uses a diffuse initial condition and the second a thin initial layer (all gas properties change across one cell thickness) and are labelled as 3DPM-Diffuse and 3DPM-Thin respectively.

In these cases a small element of perturbation is added to the pure sinosoid mode in order to attempt to replicate some variation which would occur in practice. These additional modes take the form of a numeric seeding of additional wavelengths between $16\Delta x < \lambda < 32\Delta x$ with a total power conforming to a top hat spectrum with a standard deviation of $0.1\lambda_{min}$ where λ is the wavelength.

Figure 5 shows the development of the mixing layer in 3D for three cases (compared to the 2D equivalent for reference). It is expected that the 3DSM case should behave very similarly to the 2DSM case since there is no seeding of any instability in the 3rd dimension. At late-time the numerical error will seed some instability in the 3rd direction, and the results should differ as can be seen.

Adding a perturbation increases the growth rate and this is seen in both of the perturbed modes. Adding the diffuse layer reduces the instabilities (especially due to shear and the resulting KHI) and reduces the growth rate relative to the equivalent thin layer.

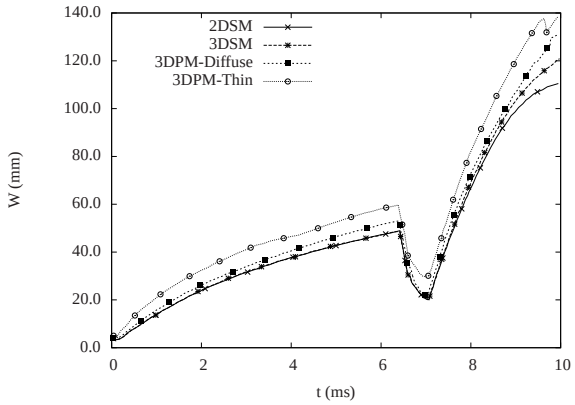

Fig. 5: Comparison of the development of the mixing layer width as a function of time for different initialisation techniques for the Collins and Jacobs test case in 3D

Iso-surfaces of volume fraction are plotted for the 3DSM and 3DPM-Diffuse cases in Fig. 6 and Fig. 7 for before reshock (5ms) and after reshock (8ms). The first figure illustrates the lack of any instability in the 3rd dimension. This result is similar to the observations made in 2D (see Fig. 4).

Comparison with the experimental images is shown in Fig. 8. Here it can clearly be seen that the low resolution does not capture all of the detail. Increasing the resolution captures more detail. Increasing the resolution yet further would alter the results again. Since there is already evidence of KHI arising in the shear layers (shown in Fig. 8e-8g) it is believed that there is no physical justification for this. Evidence of such additional instabilities at high-order of accu-

(a) 3DSM initialisation at $t = 5$ms (b) 3DPM initialisation at $t = 5$ms

Fig. 6: Volume fraction iso-surfaces (1%, 50% and 99%) immediately prior to reshock ($t = 5$ms), (a) shows the results when a 2D initialisation is used, no substantial in the 3rd arises, (b) is the results when initialised in 3D with superposition of low amplitude multi-modal perturbation (diffuse interface)

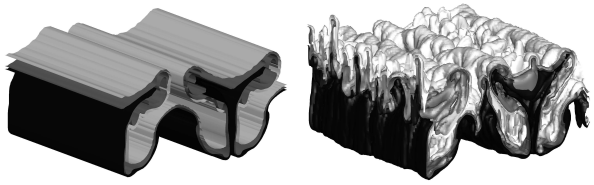

(a) 3DSM initialisation at $t = 8$ms (b) 3DPM initialisation at $t = 8$ms

Fig. 7: Volume fraction iso-surfaces (1%, 50% and 99%) immediately after reshock ($t = 8$ms), initial conditions as in Fig. 6

racy and with mesh refinement can be found in [15, 16].

The present study shows that the algorithm can be used to replicate the results of the experiment with a reasonable degree of accuracy for both stationary and moving grids.

There is further potential to improve the results. The numerical perturbation used here is an arbitary seeding as outlined previously. In practice the single-mode is initialised by oscillating the test chamber, therefore perturbations which are harmonics of the dominant single-mode are more likely to be present than the artificial values used here.

3.4 2D Study of Non-Linearity

There has been a recent strong interest in predicting the growth rate of non-linear single-mode instabilities [17–19]. Therefore the development of the mixing layer was investigated for both the initial shock wave and the reshocked case using a range of initial amplitudes. The amplitudes range from 0.5mm up to 16.0mm, in multiples of two. The results for the width of the mixing layer are shown in Fig. 9.

For the incident shock wave the initial growth rate should be given by Richtmyer's linear equation $\mathrm{d}a_0/\mathrm{dt} = k\Delta u a_0^+ \mathrm{At}^+$ [1]. Where k is the wavenumber, Δu is the change in velocity imparted by the shock, a_0 is the amplitude and At is the Atwood number. The superscript $+$ designates post-shock values ($-$ for pre-shock values).

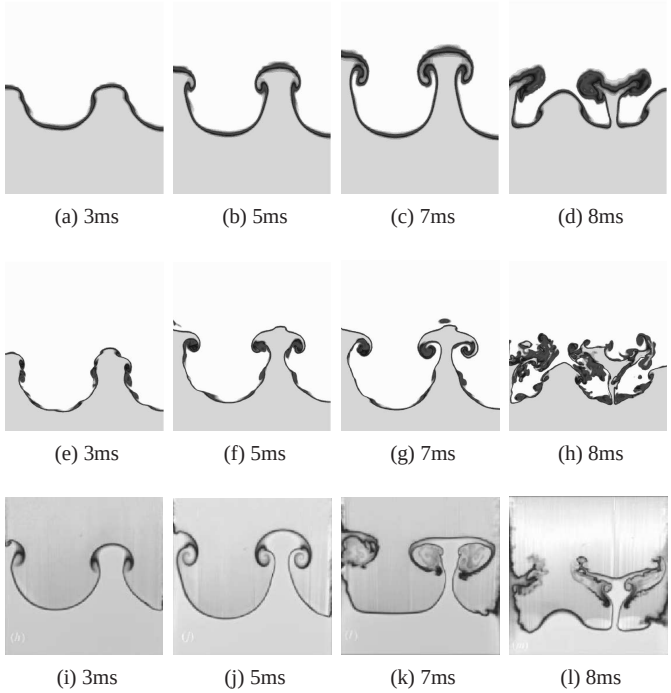

(a) 3ms (b) 5ms (c) 7ms (d) 8ms

(e) 3ms (f) 5ms (g) 7ms (h) 8ms

(i) 3ms (j) 5ms (k) 7ms (l) 8ms

Fig. 8: Slices through the central plane of the 3DPM-Diffuse simulations, the upper row (a-d) has 128 cells/wavelength, middle row (e-h) has 256 cells/wavelength and the lower row (i-l) is the experimental image ([6]). The computational results show the gradient of the volume fraction.

The post-shock amplitude can be estimated by multiplying the pre-shock amplitude by the compression factor ($\phi = \rho_1^- + \rho_2^- / \rho_1^+ + \rho_2^+$) from [20]. The initial change in velocity is estimated to be 66.7 ms^{-1} from a null case. These data are used to calculate the predicted growth rates according to Richtmyer's linear equation.

The initial growth rate is linear and proportional to ka_0 [1] whilst $ka_0 \ll 1$. From Fig. 9 the initial growth rates have been calculated and are listed in Table 1. The growth rates are calculated by straight line fitting after the initial compression and whilst the growth rate is linear. For all cases the fitting starts at $t = 0.1$ms. In the cases where $0.5\text{mm} < a_0 < 4.0\text{mm}$ the end of the range is taken as $t = 1.0$ms in the remaining two cases ($a_0 = 8.0\text{mm}, a_0 = 16.0\text{mm}$) the end of the fitting range is taken as $t = 0.3$ms. The curve fitting is done using gnuplot and the error varies from 0.06% for $a_0 = 0.5$mm to 0.28% for $a_0 = 8.0$mm (the maximum error).

Growth rates calculated in this manner are compared to the results predicted by Richtmyer's linear predictions. For the given wavenumber here linear growth is expected for $a_0 \ll 9.39$. From Table 1 it can be seen that up to an initial amplitude of 4.0mm there is variation of around $\pm$ 10% from the linear validation. It can also be seen that above this the growth rate varies significantly from the linear prediction.

Mikaelian states that for reshock of a multi-mode (MM) case, growth rates are believed to be independent of the con-

ditions at reshock [21]. Here it is investigated if the same is true for SM, and if so, at what level of non-linearity this assumption breaks down.

The SM has coherent structures and low mixing compared to the MM case and so the two are not directly comparable. Nevertheless for low-amplitude SM cases, it can be seen in Fig. 9 that varying the initial amplitude has very little impact on the post-reshock growth rate. Further Fig. 9 shows that the reshock growth rate for the lowest four amplitudes are almost identical immediately post-reshock. At the highest initial amplitudes ($a_0 = 8.0$mm and $a_0 = 16.0$mm) this is not true, the reshock occurs over a much longer period of time and the post-reshock growth rate is lower.

The two highest initial amplitude cases correspond to non-linear initial shock growth rates. It is suspected therefore that the assumption that post-reshock growth rate is independent of the initial conditions is valid for SM but only whilst the initial width is less than the wavelength of the single-mode perturbation. However for cases where the pre-reshock width is marginally greater than the wavelength of the perturbation (e.g. $a_0/\lambda = 0.136$, where $a_{pre-reshock} \approx 1.38\lambda$), the post-reshock growth is significantly slower as the mixing layer shear component becomes more significant such that the physics of the interaction is fundamentally different. In the presence of large shear layers the dominant mode will vary dramatically from the RMI to (KHI). This is a simple test case and further work is required to validate this.

The post-reshock growth rate for the smallest initial amplitude case is given as 12.232m/s by Mikaelian ($\mathrm{da/dt} = 0.28\Delta \mathrm{uAt}^{+}$ [21]). The post-reshock growth rate is 53.09m/s by Charakhch'an ($\mathrm{da/dt} = 1.25\Delta \mathrm{uAt}^{+} - \mathrm{da_0/dt}_{FirstShock}$ and [22]). These compare with 25.56m/s calculated by the code (evaluated as the gradient of Fig. 9 for $a_0 = 0.5$mm between $6.8\mathrm{ms} < t < 7.2\mathrm{ms}$. Curve fitting is done using gnuplot and yields an error of 0.09%.

There is a large discrepancy between the two results of Mikaelian and Charakhch'an owing primarily to the difference in the multiplicative factor which they use (0.28 compared to 1.25 respectively) since the pre-reshock growth rate is comparatively low. Repeating the calculation for $a_0 = 4.0$mm, considered to be the highest amplitude in this test for which the post-reshock growth rate is independent of the initial conditions, then Mikaelian predicts the same growth rate, yet now Charakhch'an yields a post-reshock growth rate of 44.05m/s. This dependence of the post-reshock growth rate on the initial condition is acting to improve the prediction for higher initial amplitudes but is not consistent with the findings that the post-reshock growth rate is independent of the initial amplitude. Thus an equation of the format of Mikaelian is appropriate for the results of amplitudes less than 8.0mm whereas after this an equation of the format of Charakhch'an may be valid.

4 Conclusions

A moving mesh algorithm has been implemented into Cranfield's in-house code CHOC, a 5^{th} order in space, 2^{nd} order in time, low Mach corrected implicit large eddy simulation solver. This is done to reduce computational time and increase accuracy in cases where there is large advection of the region of interest. In such a case the moving mesh algorithm can be used to create a clustered region containing a large number of cells which will track the aforementioned region of interest. This moving mesh algorithm has been validated against a Sod-shock tube test case and a grid study shows reasonable convergence using only 1/4 of the cells in the shock direction compared to the stationary case.

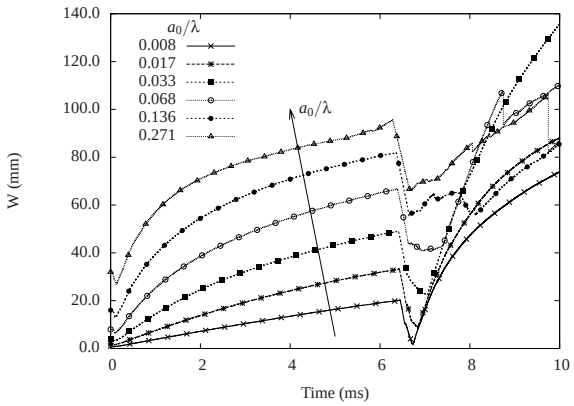

Fig. 9: Study of the effect of initial amplitude of the perturbation on the mixing layer width. Initial amplitudes are expressed as a function of the initial wavelength

a_0 (mm)	ILES $\mathrm{da_0/dt}$ (m/s)	Formula $\mathrm{da_0/dt}$ (m/s)
0.5	1.70	1.48
1.0	3.37	2.96
2.0	6.42	5.92
4.0	10.74	11.85
8.0	17.36	23.69
16.0	19.78	47.38

Table 1: Initial Growth Rates

Results are compared to the work of Collins and Jacobs [6]. Initial growth rates are consistent with Richtmyer's linear prediction for cases with low initial amplitudes. However as the initial amplitude is increased the linear relationship for the growth rates after the shock breaks down.

Investigating growth rates for linear cases after reshock shows the rates are independent of the initial amplitude (as shown by Mikaelian's multi-mode work [21]) for cases which have linear growth rates after the initial shock. However in the cases where growth rates after the first shock are non-linear the post-reshock growth rates are not independent of the initial conditions.

Single-mode 3D-RMI has also been investigated. The authors have replicated results of Collins and Jacobs and also investigated the effect of different initial layers. A thin layer

was shown to develop more rapidly than a diffuse layer and resulted in the onset of Kelvin–Helmholtz instability at an earlier time.

The succesful implementation of the moving mesh technique will facilitate the study of reshock in convergent geometries.

Achnowledgements

All simulations were ran on the Cranfield HPC facility `Astral`. This project is jointly funded by AWE and EPSRC. Many thanks to Dr. A. Aspden for his assistance with the preparation of this manuscript.

References

[1] Richtmyer, R. D., 1960. "Taylor instability in shock-acceleration of compressible fluids". *Comm. Pure. Appl. Math.*, **13**, pp. 297–319.

[2] Meshkov, E. E., 1972. "Instability of the interface of two gases accelerated by a shock wave". *Fluid Dynamics*, **4**(5), pp. 101–104.

[3] Barnes, C. W., Batha, S. H., Dunne, A. M., Magelssen, G. R., Rothman, S., Day, R. D., Elliott, N. E., Haynes, D. A., Holmes, R. L., Scott, J. M., Tubbs, D. L., Youngs, D. L., Boehley, T. R., and Jaanimagi, P., 2002. "Observation of mix in a compressible plasma in a convergent cylindrical geometry". *Phys. Plasmas*, **9**(11), pp. 4431–4434.

[4] Lindl, J. D., McCrory, R. L., and Campbell, E. M., 1992. "Progress toward ignition and burn propagation in inertial confinement fusion". *Physics Today*, **45**(9), pp. 32–40.

[5] Latini, M., Schilling, O., and Don, W. S., 2007. "High-resolution simulations and modeling of reshocked single-mode Richtmyer–Meshkov instability: Comparison to experimental data and to amplitude growth model predictions". *Phys. Fluids*, **19**.

[6] Collins, B. D., and Jacobs, J. W., 2002. "Plif flow visualization and measurement of the Richtmyer–Meshkov instability of an air/sf_6 interface". *J. Fluid. Mech*, **464**, pp. 113–136.

[7] Sod, G. A., 1978. "A survey of several finite difference methods for systems of nonlinear hyperbolic conservation laws". *J. Comput. Phys.*, **27**, pp. 1–31.

[8] Thornber, B., Bilger, R. W., Masri, A. R., and Hawkes, E. R., 2011. "An algorithm for les of premixed compressible flows using the conditional moment closure model". *J. Comput. Phys.*, **230**, pp. 7687–7705.

[9] Allaire, G., Clerc, S., and Kokh, S., 2002. "A five-equation model for the simulation of interfaces between compressible fluids". *J. Comput. Physics*, **181**, pp. 577–616.

[10] Kim, K. H., and Kim, C., 2005. "Accurate, efficient and monotonic numerical methods for multi-dimensional compressible flows part ii: Multi-dimensional limiting process". *J. Comput. Phys.*, **208**, pp. 570–615.

[11] Shu, C. W., 1988. "Total-variation-diminishing time discretizations". *SIAM J. Sci. Stat. Comput.*, **9**, pp. 1073–1084.

[12] Thornber, B., Drikakis, D., Youngs, D. L., and Williams, R. J. R., 2008. "On entropy generation and dissipation of kinetic energy in high-resolution shock-capturing schemes". *J. Comput. Phys.*, **227**, pp. 4853–4872.

[13] Thornber, B., Mosedale, A., Drikakis, D., Youngs, D. L., and Williams, R. J. R., 2008. "An improved reconstruction method for compressible flows with low mach number features". *J. Comput. Phys.*, **227**, pp. 4873–4894.

[14] Toro, E. F., 2009. *Riemann Solvers and Numerical Methods for Fluid Dynamics*, 3 ed. Springer, Berlin.

[15] Mosedale, A., and Drikakis, D., 2007. "Assessment of very high order of accuracy in implicit les models". *ASME J. Fluid. Eng.*, **129**, pp. 1497–1503.

[16] Liska, R., and Wendroff, B., 2003. "Comparison of several difference schemes on 1d and 2d test problems for the euler equations". *SIAM J. Sci. Comput.*, **25**(3), pp. 995–1017.

[17] Akshay, A. A., Ristorcelli, J. R., and Grinstein, F. F., 2011. "The bipolar behavior of the Richtmyer–Meshkov instability". *Phys. Fluids*, **23**.

[18] Balakumar, B. J., Orlicz, G. C., Tomkins, C. D., and Prestridge, K. P., 2008. "Simultaneous particle-image velocimetry-planar laser-induced fluorescence measurements of Richtmyer–Meshkov instability growth in a gas curtain with and without reshock". *Phys. Fluids*, **20**(12), pp. 124103:1–124103:13.

[19] Thornber, B., Drikakis, D., Youngs, D. L., and Williams, R. J. R., 2012. "Physics of the single-shocked and reshock Richtmyer–Meshkov instability". *J. Turb.*, **12**(N10).

[20] Thornber, B., Drikakis, D., Youngs, D. L., and Williams, R. J. R., 2010. "The influence of initial conditions on turbulent mixing due to Richmyer–Meshkov instability". *J. Fluid. Mech.*, **654**, pp. 99–139.

[21] Mikaelian, K. O., 1989. "Turbulent mixing generated by Rayleigh–Taylor and Richtmyer–Meshkov instability". *Physica. D*, **36**, pp. 343–357.

[22] Charakhch'an, A. A., 2000. "Richtmyer–Meshkov instability of an interface between two media due to passage of two succesive shocks". *J. Appl. Mech. Tech. Phys*, **41**(1), pp. 23–31.